Molecular gas and dust in the highly magnified *z* ~ 2.8 galaxy behind the Bullet Cluster

D. Johansson[1], C. Horellou[1], O. Lopez-Cruz[2], S. Muller[1], M. Birkinshaw[3], J. H. Black[1], M. N. Bremer[3],
W. F. Wall[2], F. Bertoldi[4], E. Castillo[2], and H. J. Ibarra-Medel[2]

[1] Onsala Space Observatory, Department of Earth and Space Sciences, Chalmers University of Technology, 439 92 Onsala, Sweden
e-mail: daniel.p.johansson@chalmers.se
[2] Instituto Nacional de Astrofísica, Optica y Electrónica (INAOE), Tonantzintla, 72840 Puebla, Mexico
[3] HH Wills Physics Laboratory, University of Bristol, Tyndall Avenue, Bristol BS8 1TL, UK
[4] Argelander-Institut für Astronomie, Auf dem Hügel 71, 53121 Bonn, Germany

ABSTRACT

Context. The gravitational magnification provided by massive galaxy clusters makes it possible to probe the physical conditions in distant galaxies that are of lower luminosity than those in blank fields and likely more representative of the bulk of the high-redshift galaxy population.
Aims. We aim to constrain the basic properties of molecular gas in a strongly magnified submm galaxy located behind the massive Bullet Cluster (1E 0657-56). This galaxy (SMM J0658) is split into three images, with a total magnification factor of almost 100.
Methods. We used the Australia Telescope Compact Array (ATCA) to search for $^{12}CO(1–0)$ and $^{12}CO(3–2)$ line emission from SMM J0658. We also used the SABOCA bolometer camera on the Atacama Pathfinder EXperiment (APEX) telescope to measure the continuum emission at 350 μm.
Results. CO(1–0) and CO(3–2) are detected at 6.8σ and 7.5σ significance when the spectra toward the two brightest images of the galaxy are combined. From the CO(1–0) luminosity we derive a mass of cold molecular gas of $(1.8 \pm 0.3) \times 10^9 \, M_\odot$, using the CO to H_2 conversion factor commonly used for luminous infrared galaxies. This is $45 \pm 25\%$ of the stellar mass. From the width of the CO lines we derive a dynamical mass within the CO-emitting region L of $(1.3 \pm 0.4) \times 10^{10} (L/1 \, kpc) \, M_\odot$. We refine the redshift determination of SMM J0658 to $z = 2.7793 \pm 0.0003$. The CO(3–2) to CO(1–0) brightness temperature ratio is $0.56^{+0.21}_{-0.15}$, which is similar to the values found in other star-forming galaxies. Continuum emission at 350 μm from SMM J0658 was detected with SABOCA at a signal-to-noise ratio of 3.6. The flux density is consistent with previous measurements at the same wavelength by the Herschel satellite and BLAST balloon-borne telescope. We study the spectral energy distribution of SMM J0658 and derive a dust temperature of 33 ± 5 K and a dust mass of $1.1^{+0.8}_{-0.3} \times 10^7 \, M_\odot$.
Conclusions. SMM J0658 is one of the least massive submm galaxies discovered so far. As a likely representative of the bulk of the submm galaxy population, it is a prime target for future observations.

Key words. submillimeter: galaxies – infrared: galaxies – cosmology: observations – gravitational lensing: strong

1. Introduction

Molecular gas is the raw material from which stars form. Determining the amount of molecular material and the physical conditions of the molecular interstellar medium in distant galaxies is important to understand the cosmic history of star-formation and the evolution of galaxies (see reviews by Solomon & Vanden Bout 2005; Walter et al. 2010). Since the first detection of carbon monoxide in a high-redshift galaxy twenty years ago (IRAS F10214+4724 at z = 2.3; Brown & Vanden Bout 1991; Solomon et al. 1992), CO and other molecules have been detected in different types of distant galaxies, indicating the presence of significant reservoirs of molecular gas: $>10^8 \, M_\odot$ in Lyman-break galaxies (e.g., Stanway et al. 2008; Riechers et al. 2010), larger amounts (a few times $10^9 \, M_\odot$ in some submillimeter-faint radio-selected starburst galaxies (e.g. Chapman et al. 2008), and even larger amounts ($>10^{10} \, M_\odot$) in near-infrared–selected star-forming galaxies (e.g., Dannerbauer et al. 2009), submillimeter galaxies (SMGs, e.g., Greve et al. 2005; Daddi et al. 2009; Ivison et al. 2011), and in quasars and quasi-stellar objects (e.g., Alloin et al. 2007; Coppin et al. 2008). The SMG population contains extreme objects: high-redshift

dust-obscured star-forming galaxies with rest-frame far-infrared luminosities larger that $10^{12} \, L_\odot$ and star-formation rate of about $1000 \, M_\odot \, yr^{-1}$ (e.g. Smail et al. 1997; Blain et al. 2002).

Whereas the brightest SMGs contribute largely to the star-formation rate in the Universe, they are not representative of the high-redshift SMG population as a whole: number counts indicate a steep increase of the SMG population with decreasing flux density, S_ν: the space density of SMGs is about $10^4 \, deg^{-2}$ for sources with $S_\nu > 1$ mJy (e.g. Hughes et al. 1998; Chapman et al. 2001; Smail et al. 2002), and it is about ten times larger for galaxies with $S_\nu > 0.1$ mJy (e.g. Knudsen et al. 2008). The abundant sub-mJy population is difficult to detect in observations of relatively poor angular resolution ($15''–30''$) because of confusion noise. Most detections so far were possible because of gravitational lensing by a foreground galaxy or a galaxy cluster, that not only brightens a source but also provides an effective increase in angular resolution, which lowers the confusion limit (e.g. Smail et al. 1997, 2002; Chapman et al. 2002; Knudsen et al. 2005, 2006, 2008; Johansson et al. 2010; Wardlow et al. 2010; Rex et al. 2009; Egami et al. 2010; Johansson et al. 2011). With the Atacama Large Millimeter/Submillimeter Array

(ALMA), the Large Millimeter Telescope (LMT) and the Cerro Chajnantor Atacama Telescope (CCAT), the situation will be transformed, making it possible to observe faint sources directly. Until then, observations of highly magnified sources provide a first glimpse into the bulk of the SMG population.

Few sub-mJy SMGs have been discovered so far: there are seven in Knudsen et al. (2008)'s sample, and five in Cowie et al. (2002)'s sample. Smail et al. (2002) estimated number counts down to 0.25 mJy, but the low-end counts were inferred from a Monte Carlo analysis and lower limits on the magnification of several faint sources. To allow detection in a reasonable amount of observing time, the submm flux density (before correcting for magnification) should preferably be larger than 10 mJy, implying a magnification higher than 10. One SMG that satisfies those criteria is the galaxy at $z \sim 2.5$ lensed by the massive cluster Abell 2218 (Kneib et al. 2004; Kneib et al. 2005). This source has a total magnification of 45 and an intrinsic submm flux of 0.8 mJy. CO(3–2) was detected in all three images and CO(7–6) in the brightest one, and a gas mass of 4.5×10^9 and a star formation rate of about 500 $M_\odot$ yr^{-1} were inferred (Kneib et al. 2005).

Another sub-mJy SMG is the recently discovered galaxy SMM J065837.6–555705 (hereafter SMM J0658) at $z = 2.79$ situated near the caustic line of the Bullet Cluster (1E 0657-56) at $z \sim 0.3$, and magnified about 100 times (Bradač et al. 2006; Wilson et al. 2008; Gonzalez et al. 2009; Gonzalez et al. 2010, hereafter G10; Johansson et al. 2010). It is the subject of this paper. The galaxy classifies as a luminous infrared galaxy (LIRG), with an intrinsic far-infrared luminosity of a few times $10^{11} L_\odot$. The source was also detected by BLAST and Herschel; its infrared spectral energy distribution is consistent with that of a dusty starburst galaxy (Rex et al. 2009, 2010). It is the brightest source in our APEX LABOCA 870 μm survey of gravitationally lensed submm galaxies (Johansson et al. 2011), in which it was detected with a significance of $\sim 30\sigma$. When corrected for the gravitational magnification, it appears to be one of the intrinsically faintest submm galaxies detected so far ($S_{870\mu m} \sim 0.5$ mJy). The galaxy is strongly lensed, and three images, A through C, were identified in infrared *Spitzer* images (Gonzalez et al. 2009, G10). Images A and B are separated by 8″ and have individual magnification factors of ~ 30 and ~ 70 (G10). The third image, C, lies 30″ away from the centroid of images A and B, and its magnification factor is smaller (<10), making it too faint for detection in the submm and mm observations discussed here. Recently, a faint arc extending between images A and B was discovered in *Hubble* Space Telescope (HST) near-infrared images (G10). G10 also presented the first spectroscopic redshift of SMM J0658, $z = 2.791 \pm 0.007$, derived from polycyclic aromatic carbon (PAH) bands. They also reported the detection of two rotational lines of H$_2$, and derived a warm molecular gas mass of $2.2^{+17}_{-0.8} \times 10^8 (\mu_{AB}/100)^{-1} M_\odot$, where μ_{AB} is the total magnification, and a gas temperature of 377^{+68}_{-85} K.

In this paper, we present the first detections of CO(1–0) and CO(3–2) in SMM J0658. The observations were done with the Australia Telescope Compact Array (ATCA). We use the CO detections to constrain the basic properties of the cold molecular gas in SMM J0658. To complement the existing Herschel observations we also present APEX SABOCA observations of the 350 μm continuum that we use to quantify the dust properties.

Throughout the paper, we adopt the following cosmological parameters: a Hubble constant $H_0 = 71$ km s^{-1} Mpc^{-1}, a matter density parameter $\Omega_0 = 0.27$, and a dark energy density parameter $\Omega_{\Lambda 0} = 0.73$. In this cosmology, $z = 2.8$ corresponds to an angular-diameter distance of 1650 Mpc, a luminosity distance of 23 800 Mpc and a scale of 8.0 kpc/arcsec[1].

2. Observations and data reduction

2.1. SABOCA (350 μm)

We observed SMM J0658 with the Submillimeter APEX Bolometer Camera (SABOCA), a facility instrument operating in the 350 μm atmospheric window on the Atacama Pathfinder EXperiment (APEX[2]) telescope in Chile (Güsten et al. 2006). SABOCA consists of 39 bolometers, has an instantaneous field-of-view of 1′.5, and the main beam has a full width at half maximum (FWHM) of 7″.8 (Siringo et al. 2010).

SMM J0658 was observed in 2010, on June 2nd and 9th and on August 2nd and 5th, as part of observing program O-085.F-9308A. The total observing time was 7.4 h, out of which approximately 5.4 h were spent on source and the remaining time was used for calibration scans and pointing. Pointing scans were performed every ~ 30 min and the pointing corrections were usually smaller than 2″. Skydips (fast scans in elevation at constant azimuthal angle) were performed at least once during each observing session to estimate the atmospheric opacity. The weather conditions at the time of the observations were good, with a median precipitable water vapor level of 0.46 mm, and standard deviation of 0.05 mm. The derived atmospheric optical depths were between 0.7 and 1.0. SABOCA was used in scanning mode to yield a constant noise level within the central arcminute of the map. In total, 42 scan maps were obtained.

The data were reduced with the `Crush` software[3] (Kovács 2008), following the procedure outlined by Johansson et al. (2009).

2.2. ATCA (3 mm and 7 mm)

We observed SMM J0658 with the Australia Telescope Compact Array (ATCA[4]) in October and November 2010 and in March 2011 with the aim to detect the two rotational lines of carbon monoxide (^{12}C^{16}O) redshifted within the ATCA frequency coverage: namely, the $J = 1 \rightarrow 0$ and $J = 3 \rightarrow 2$ lines. For gas at $z \sim 2.8$ these lines are redshifted into the 7 mm and 3 mm bands. The ATCA Compact Array Broadband Backend (CABB) correlator has two spectral bands with 2 GHz bandwidth each, which can be arranged in various configurations. The correlator was set up in the CFB 1M-0.5k mode yielding 2049 channels each with spectral width 1 MHz. In the 7 mm band, where the CO(1–0) line is redshifted to 30.41 GHz, we centered the band on 30.5 GHz, and covered frequencies between 29.5 and 31.5 GHz. In the 3 mm band the CO(3–2) line is redshifted to 91.23 GHz, and we centered the first band at 91 GHz, covering the range between 90 and 92 GHz. Because ATCA allows for another band to be observed simultaneously, we decided to center it at 93.8 GHz to search for the lines of hydrogen cyanide, HCN,

---

Table 1. Parameters of the ATCA observations and data.

Phase center (J2000):	
Right ascension	06:58:37.62
Declination	-55:57:04.8
3 mm band	
Central observing frequency	30.5 GHz
Configuration	214H
Bandpass calibrator	1921–293
Phase calibrator	0537–441
Primary flux calibrator	Uranus
Primary beam FWHM	38″
Synthesized beam[1]	$2\rlap{.}''1 \times 1\rlap{.}''7$; 82°
Channel velocity width	3.3 km s^{-1}
Final velocity resolution	80 km s^{-1}
Noise level[2]	1.6 mJy
7 mm band	
Central observing frequency	91 GHz
Configuration	750A and 750D
Bandpass calibrator	0537–441
Phase calibrator	0724–47
Primary flux calibrator	Uranus
Primary beam FWHM	110″
Synthesized beam[1]	$5\rlap{.}''5 \times 1\rlap{.}''6$; -8°
Channel velocity width	9.8 km s^{-1}
Final velocity resolution	80 km s^{-1}
Noise level[2]	0.85 mJy

Notes. [1] Beam full-width at half maximum (FWHM) and position angle, measured counter-clockwise from the north. [2] Measured in the final spectra, and referring to a resolution element of 80 km s^{-1}.

redshifted to 93.53 GHz, and the formyl ion HCO$^+$, redshifted to 94.13 GHz. The rest frequencies of the molecular transitions are listed in Table 2.

The 7 mm observations were done on November 11–12, 2010. The array was in the 750A configuration and all six antennas were available. Additional 7 mm observations were carried out on 2011 March 4 and 7, on Director's Discretionary Time, when the array was in the 750D configuration. The total observing time was 21 h.

The 3 mm observations were done on October 16–17, 2010, in the H214 array configuration in good weather conditions. On the first day, antenna 4 was taken offline, so most of the observations were done with four antennas. The total observing time was 10 h.

The parameters of the ATCA observations are summarized in Table 1. The incomplete *uv*-coverage of the 7 mm observations results in an elongated beam in the north-south direction (see Table 1, and Figs. 2 and 3).

We used the `Miriad` software package to reduce the data. We calibrated each day and frequency band separately, using a standard calibration procedure. After initial flagging, the bandpass solution was derived and applied to all sources, followed by gain and flux calibration. The different calibrators we used are listed in Table 1. The data for each band were combined to the final 3 mm and 7 mm *uv*-datasets for SMM J0658. Images were obtained by Fourier-transform of these visibility sets, using natural weighting.

At 7 mm we discarded the data from all baselines including the most remote antenna (located 6 km away from the center of the array) because of significant phase noise on those baselines. We also flagged all data during the second half of the first night, when the stability was poor due to rainfall. For the CLEANing procedure, we selected regions around the two images of the
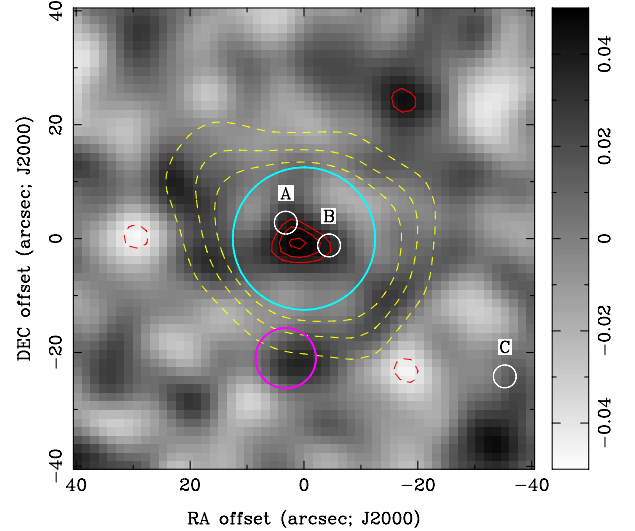

Fig. 1. Central region of the SABOCA 350 μm map. The grayscale is in Jy/beam. The red contours show significance levels of ±2.5, 3.0 and 3.5σ (positive values as solid lines and negative values as dashed lines). SMM J0658 is detected at the center of this image at 3.6σ significance. The white circles indicate the positions of the three *Spitzer* images A, B and C (Gonzalez et al. 2009). The magenta circle has a diameter of $10\rlap{.}''6$, the FWHM of the SABOCA image; it is located at the position of an infrared-bright elliptical galaxy at $z = 0.35$ (Rex et al. 2010) which is not detected by SABOCA, as expected (the continuum from this galaxy is detected in the ATCA 7 mm observations and used to assess the astrometry of the CO(1–0) map, see Sect. 3.2.1). The yellow dashed lines correspond to the 3, 6 and 9σ levels of the LABOCA 870 μm detection. The source was detected by Herschel (Rex et al. 2010): the cyan circle shows the size of the Herschel beam at 350 μm (FWHM of 25″). The coordinates of the (0, 0)-position are the same as those of the phase center of the ATCA observations, which are listed in Table 1.

galaxy and around a bright point source about 20 arcseconds south of them. This source is discussed in Sect. 3.2.1.

At 3 mm we corrected for the opacity of the atmosphere, phase differences between antennas, and interpolated between the measured system temperatures. Imaging the 3 mm data gave a map without noticeable artefacts and no CLEANing of the 3 mm cube was needed.

3. Results

3.1. 350 μm continuum

The 350 μm SABOCA map is shown in Fig. 1, overlaid with contours of the signal-to-noise map. The symbols indicate the location of the infrared counterpart. SMM J0658 is detected at 350 μm with a peak signal-to-noise ratio of 3.6. The integrated flux density is 75 ± 21 mJy, where the uncertainty is the 1σ noise level estimated from the data. It does not include the systematic uncertainty in absolute flux calibration, which is $\sim$20% (Siringo et al. 2010).

We now compare our measurement to previous detections at 350 μm. Rex et al. (2010) measured a flux density of 98.6 ± 3.9 mJy, which does not include calibration uncertainties or confusion noise, in the Herschel beam of 25″. The absolute flux calibration for the SPIRE instrument operating at 350 μm is better than 15% (Griffin et al. 2010). Previously, Rex et al. (2009) had measured a flux density at the same wavelength of 96 ± 27 mJy with BLAST, for which the absolute flux calibration is better

Channel maps at 3 mm (redshifted CO(3–2))

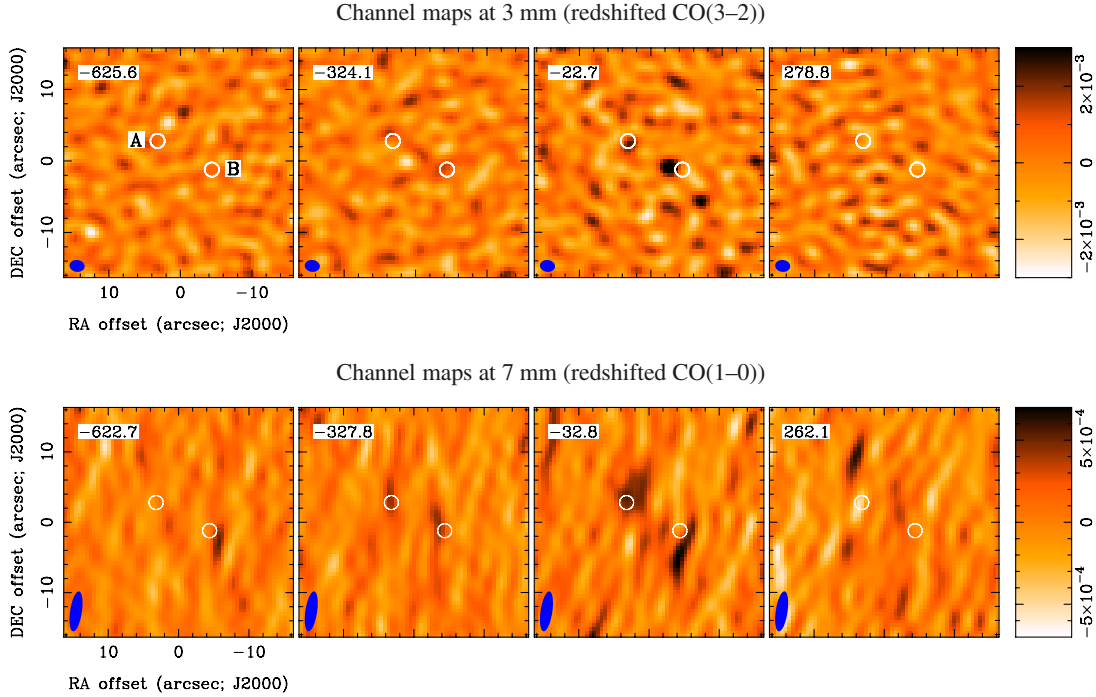Channel maps at 7 mm (redshifted CO(1–0))

Fig. 2. Channel maps around the CO lines. The white circles indicate the positions of the *Spitzer* images A and B (Gonzalez et al. 2009). Each channel has a width of ~300 km s^{-1} and the central velocity of each channel is noted in the upper left corners. The beam is shown in the bottom left corner and the color bars show the range of surface brightnesses, in Jy beam^{-1}. *Top row*: channel maps at 3 mm, the band into which the CO(3–2) line is redshifted. Emission is clearly seen near image B (the western image) in the *third panel*. Faint emission near image A is seen in the *third panel*. *Bottom row*: channel maps at 7 mm, the band into which the CO(1–0) line is redshifted. Emission is detected close to images A and B and is best seen in the third panel. The continuum source discussed in Sect. 3.2.1 lies outside the field displayed here. The velocity $v = 0$ corresponds to a redshift of $z = 2.7793$. Positional offsets refer to the phase center in Table 1.

Table 2. Integrated flux densities and upper limits on interesting molecular transitions in the ATCA bands.

Line	ν_{rest} [GHz]	Image A	Image B	Image A+B	Image A+B $L_{line} (\mu_{AB}/100)^{-1}$ [10^8 K km s^{-1} pc^2]	Flux B/A
		⋯⋯⋯⋯⋯ Integrated flux ⋯⋯⋯⋯⋯ [Jy km s^{-1}]				
^{12}CO(1–0)	115.271	0.34 ± 0.07	0.29 ± 0.07	0.63 ± 0.10	22.6 ± 3.6	$0.9^{+0.5}_{-0.3}$
^{12}CO(3–2)	345.796	0.94 ± 0.35	2.25 ± 0.35	3.18 ± 0.50	12.7 ± 2.0	$2.4^{+1.3}_{-0.7}$
HCN(4–3)	354.460	⋯	⋯	<0.7	<2.7	⋯
HCO$^+$(4–3)	356.734	⋯	⋯	<0.7	<2.7	⋯
CS(7–6)	342.883	⋯	⋯	<0.5	<2.0	⋯
Brightness temperature ratios (r_{31})						
		$0.31^{+0.22}_{-0.14}$	$0.86^{+0.45}_{-0.28}$	$0.56^{+0.21}_{-0.15}$		

Notes. Uncertainties correspond to the 1σ level, and upper limits are quoted for 3σ. Integrated flux values are derived from fitting point sources at the positions of images A and B in the CO(1–0) and CO(3–2) maps collapsed for velocities between -350 and $+170$ km s^{-1}, as described in the text. This velocity range was determined from the spectral extent of the CO(3–2) spectrum. Measuring the fluxes in the individual and combined spectra yields results within 10% of those reported here.

than 10%–13%. The Herschel, BLAST and SABOCA measurements are consistent when calibration uncertainties and confusion noise are taken into account. The SABOCA observations confirm that the emission comes from SMM J0658.

We use the SABOCA and Herschel measurements in the analysis of the spectral energy distribution (Sect. 4.1).

3.2. CO lines

3.2.1. Astrometry of ATCA data

The presence of a bright point-like continuum source in the field of view of the 7 mm data allows us to assess the astrometry of the 7 mm map. The source is located at RA 06:58:37.99, Dec –55:57:25.8, which is 21″ south of SMM J0658, and it is shown in yellow contours in Fig. 3. The elongated 7 mm synthesized beam is shown in the bottom left corner. When the entire 7 mm dataset is collapsed in velocity/frequency the signal-to-noise of this source is around 50. The source is located 1.1″ southeast of a strong radio source detected by Liang et al. (2000) in cm-wave ATCA observations (their source A). Its flux density S_ν at 7 mm is 1.02 ± 0.03 mJy, and together with the cm detections we derive a centimeter-to-millimeter spectral index α of -1.02 ± 0.05 ($S_\nu \propto \nu^\alpha$), indicative of a radio synchrotron emission mechanism.

The extrapolated continuum flux density in the 3 mm band is 0.3 mJy. This is below the noise level at the edge of the primary
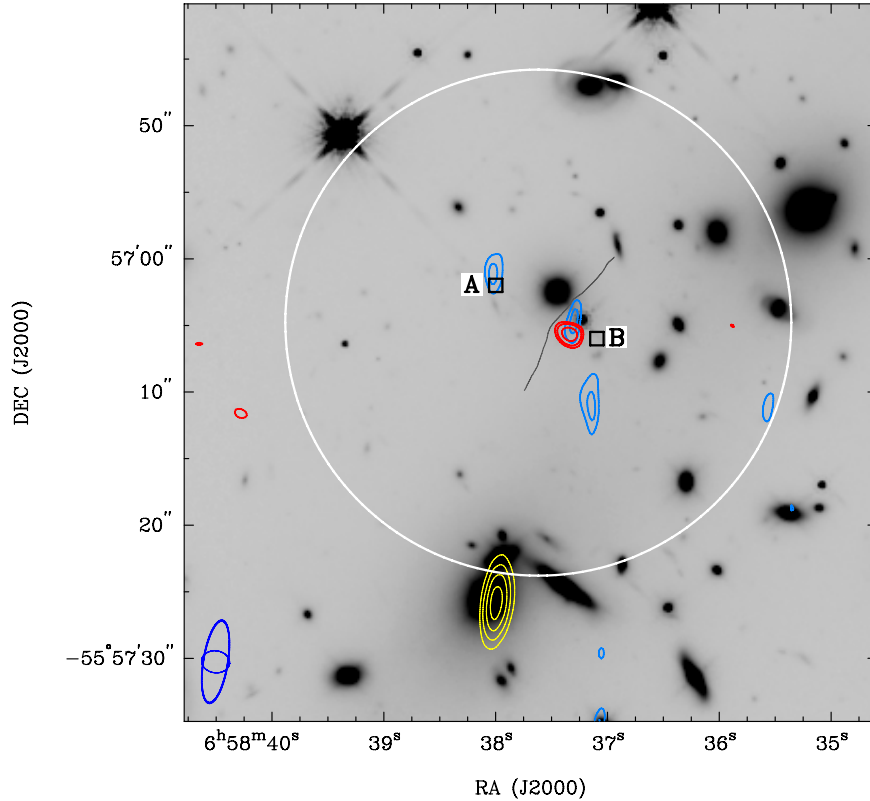
Fig. 3. HST/WFC3 1.6 μm image of the region around SMM J0658. The blue contours show the CO(1–0) integrated intensity of both images of SMM J0658 and, red contours show the CO(3–2) integrated intensity. The 7 mm continuum emission from the $z = 0.35$ galaxy to the south is indicated by yellow contours. The contour levels of the CO images are 3, 3.5 and 4σ, and those of the continuum image are 7, 9, 11 and 13σ. The two black squares indicate the locations of the two infrared *Spitzer* images, A to the east and B to the west (Gonzalez et al. 2009). CO(1−0) emission is seen at the positions of both images, but CO(3−2) emission is only seen at image B. The low significance of CO(3−2) at image A can also be seen in the spectrum (Fig. 4) The gray line between images A and B is the critical line, derived from the lensing model for a source redshift of $z = 2.7$ (Gonzalez et al. 2009), very similar to the redshift derived from the CO observations. The white circle shows the extent of the ATCA FWHM primary beam for the CO(3−2) observations; the primary beam at 7 mm is larger than the field displayed here. The offsets seen between the various components are discussed in Sect. 4.3.

beam of the 3 mm map, where the source lies, and it is not detected.

In the HST near-infrared map (see Fig. 3), the radio source has a counterpart in an elliptical galaxy which is a member of the structure at $z = 0.35$ behind the Bullet Cluster (Rex et al. 2010). The near-infrared galaxy is located 0.7″ northeast of the radio source. The offsets between the radio source and the $z = 0.35$ galaxy in *Spitzer* maps are also <1″. The offsets to the infrared and infrared counterparts of the source implies that the astrometry in our 7 mm map is better than ∼1″.

In order to remove sidelobe effects from the continuum source, we subtracted it in the Fourier plane using the Miriad task `uvlin`. Imaging this modified dataset produced an improved CO(1–0) map of SMM J0658.

3.2.2. The CO maps

The CO maps are shown in Fig. 2 (channel maps) and Fig. 3 (contours of CO integrated intensity overlaid on an HST image in grayscale).

In the channel maps, which are averaged over ∼300 km s^{-1}, emission near the *Spitzer* images A and B is best seen in the third panels. In the 3 mm maps, CO(3–2) is detected at image B in the channel centered near 0 km s^{-1}. A faint peak is seen near image A. The distance between the two positions is smaller than that between the *Spitzer* images A and B. In the

7 mm maps, CO(1–0) is detected close to images A and B in the channel centered near 0 km s^{-1} and also in the one centered near −300 km s^{-1}, although with lower significance. The positions of the CO(1–0) emission are slightly offset to the north and south of the *Spitzer* images A and B.

We selected the velocity range from −350 km s^{-1} to +170 km s^{-1} to make images of the integrated CO emission. This is the approximate range from which the CO(3–2) emission originates (see Fig. 4). We measured the integrated intensity of both transitions and both images in the maps, by fitting the sum of two point sources convolved with the synthesized beam in each map at the positions discussed above. Measuring the flux in the extracted spectra instead yield results which agree within ∼10%. CO(1–0) emission is detected near both *Spitzer* images. CO(3–2) emission, on the other hand, is clearly detected only near image B.

Continuum emission at 7 mm is seen from the $z \sim 0.35$ elliptical galaxy to the south. Offsets between the ATCA and *Spitzer* counterparts of SMM J0658 are discussed in Sect. 4.3.

In Table 2 we list integrated fluxes and luminosities for both CO lines, measured from the integrated images. The relation between integrated flux F and line luminosity L_{line} is

$$L_{\text{line}} = 3.25 \times 10^7 \ (F/\mu_{\text{AB}}) \ \nu_{\text{obs}}^{-2} \ D_{\text{L}}^2 (1 + z)^{-3} \qquad (1)$$

where ν_{obs} is the observed (sky) frequency (in GHz) of the spectral line and D_{L} is the luminosity distance (in Mpc)

(Solomon & Vanden Bout 2005). The dependence on the magnification value is explicitly included. The CO line luminosities derived from this equation are expressed in units of K km s^{-1} pc^2.

3.2.3. The CO spectra

The spectra extracted from the positions of images A and B discussed in the previous section are displayed in Fig. 4. In the two upper panels we show the spectra from the CO(3–2) and CO(1−0) transitions toward both images. Assuming that the spectra toward images A and B originate from the same galaxy, we can increase the signal-to-noise ratio of the detections by simply adding the spectra toward the two images. The total CO(1–0) and CO(3–2) spectra are shown in the lowest panel of Fig. 4.

In the combined spectra (image A + B), CO(3–2) is detected at 7.5σ significance, and CO(1–0) is detected at 6.8σ significance.

We used the CO(3–2) spectrum combined for images A and B to determine the redshift of the galaxy and measure the linewidth by fitting a single Gaussian. We derived a redshift $z = 2.7793 \pm 0.0003$. This value is consistent with the CO(1−0) detection, and slightly lower than the value measured by G10 (see Fig. 4). This value is adopted in all z-dependent results.

The resulting Gaussian has a velocity width of $\Delta V_{\rm FWHM} = 240 \pm 40$ km s^{-1}. The fit is adequate, with a reduced χ^2 of 1.2 and a probability to exceed of 20%. The linewidth is used to estimate the dynamical mass in Sect. 4.2.

A brightness temperature ratio $r_{31} = 0.56^{+0.21}_{-0.15}$ is found between the CO(3–2) and CO(1–0) lines. This is within the range of values found in those star-forming galaxies where both CO lines have been observed. In a sample of 49 local LIRGs, Leech et al. (2010) found a median brightness temperature ratio $r_{31} = 0.49$, and ranging between $0.2 < r_{31} < 0.7$. Few high-redshift galaxies have been detected in both the CO(1–0) and CO(3–2) line; this is because observation of the CO(1–0) line in the $z \sim 2$–3 redshift range has become possible only recently, with the Expanded Very Large Array (e.g. Ivison et al. 2011), the CABB correlator of the ATCA, or the Z-receiver at the Green Bank Telescope. In those SMGs where both CO(1−0) and CO(3−2) have been detected, r_{31}-values are similar to that derived for SMM J0658. Swinbank et al. (2010) reported $r_{31} \sim 0.7$ in the lensed SMG SMMJ2135-0102 at $z \sim 2.3$ and Harris et al. (2010) found $r_{31} = 0.68 \pm 0.08$ in a sample of three SMGs at $z \sim 2.5$. Ivison et al. (2011) found $\langle r_{31} \rangle = 0.55 \pm 0.05$ in four SMGs at $z = 2.2$–2.5. Observations of additional rotational transitions of CO are required to further constrain the excitation conditions in SMM J0658.

3.3. On the non-detection of dense gas tracers

The large bandwidth of the ATCA correlator provides coverage of other interesting molecular lines (HCN(4–3), HCO$^+$(4–3) and CS(7–6)), and upper limits on their integrated fluxes and luminosities are given in Table 2. These molecules have larger critical densities than CO, and trace denser gas. The flux ratio between CO(3–2) and HCO$^+$(4–3) is >20 in the Cloverleaf quasar (Weiß et al. 2003; Riechers et al. 2011). In their study of the lensed SMG SMMJ2135-0102, Danielson et al. (2010) detected HCN(3–2), and found a flux density ratio of 1/10 compared to CO(3–2). Their non-detections of HCO$^+$(4–3) and CS(7–6) also indicated flux ratios <1/10 compared with CO(3–2). This is similar to our limits on the ratios between CO(3–2) and HCN, HCO$^+$ and CS, and thus our non-detections are not surprising.
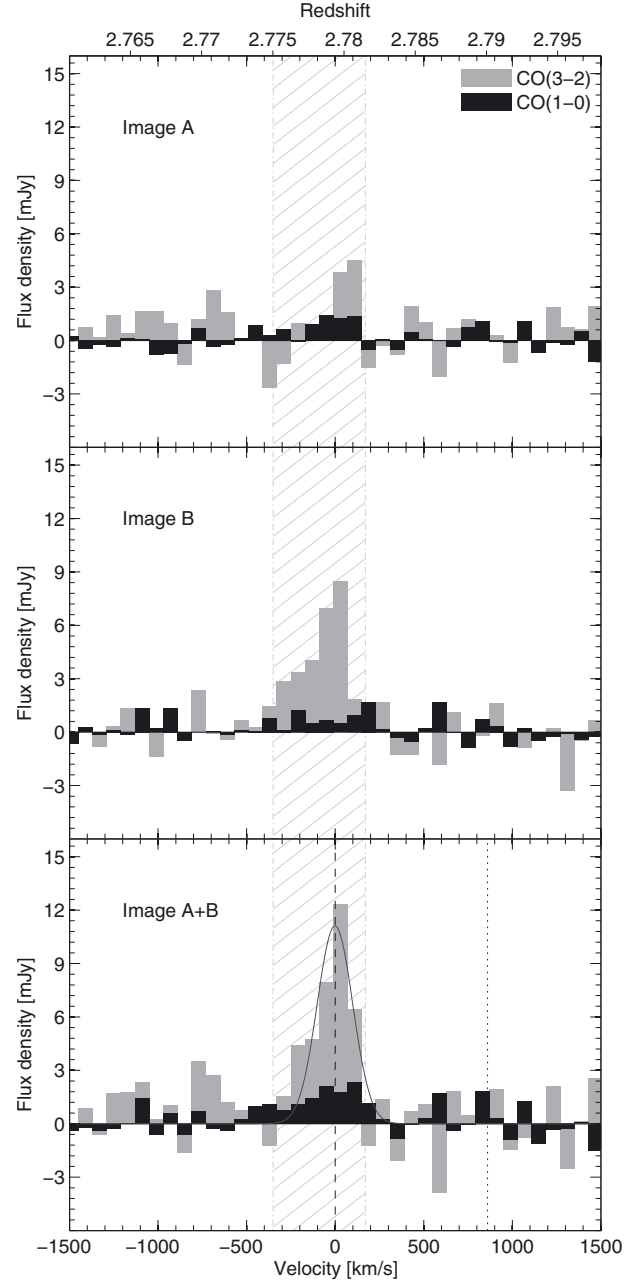
Fig. 4. CO(1–0) and CO(3–2) spectra as functions of velocity and redshift, showing that both emission lines originate from gas at the same systemic velocity. The *upper and middle panels* show individual spectra toward the positions of image A and B. The *lower panel* shows the combined spectrum and the Gaussian model fitted to the CO(3–2) spectrum. The redshift derived from the CO lines is indicated ($z = 2.7793$, dashed line); it differs slightly from the redshift derived by G10 from PAH lines ($z \sim 2.79$, dotted line). The hashed region shows the spectral extent of the integrated images shown as contours in Fig. 3, from which we measured the flux of the CO lines. This velocity interval was determined from the combined CO(3–2) spectrum. The velocity resolution of both spectra is 80 km s^{-1}.

4. Discussion

4.1. Dust properties

The FIR/submm continuum emission of SMM J0658 has been thoroughly studied and it is established that SMM J0658 is a LIRG with a far-infrared luminosity $L_{\rm FIR} < 10^{12} L_\odot$.
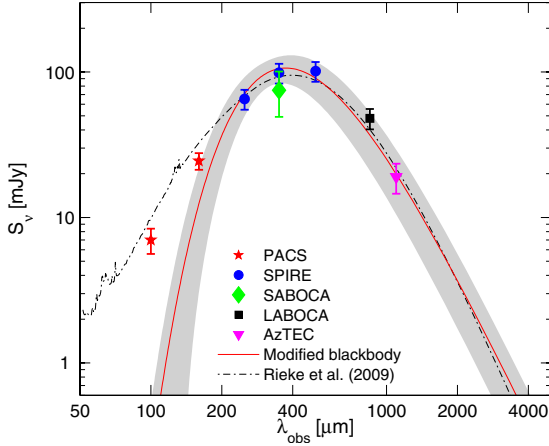
Fig. 5. Spectral energy distribution of SMM J0658. The solid line corresponds to the best-fit model of Eq. (2) to the long-wavelength points ($\lambda \geq 250\ \mu$m), with $\beta = 1.5$, and the shaded area is the 95% confidence interval. The black curve is the LIRG template with far-infrared luminosity $2 \times 10^{11}\ L_\odot$ from Rieke et al. (2009), magnified by a factor $\mu_{AB} = 100$. The data points were taken from Rex et al. (2010) (PACS and SPIRE), this work (SABOCA), Johansson et al. (2011) (LABOCA) and Wilson et al. (2008) (AzTEC).

(Wilson et al. 2008; Rex et al. 2009; Johansson et al. 2010; Rex et al. 2010; Pérez-González et al. 2010). From the continuum data that include our SABOCA 350 μm measurement and the LABOCA 870 μm measurement of Johansson et al. (2010) we constructed the FIR/submm spectral energy distribution (SED) displayed in Fig. 5.

Rex et al. (2009) used the continuum data measured by BLAST and AzTEC to estimate a dust temperature in SMM J0658 of 32 K. In the analysis of the more sensitive observations by the SPIRE and PACS instrument on the Herschel satellite, Rex et al. (2010) fitted SED models but did not derive a dust temperature. To calculate the dust temperature we therefore fitted a modified blackbody curve to the SED, following the approach in Rex et al. (2009). We adopted the following functional form of the SED

$$S_\nu = A \left(\frac{\nu}{\nu_0} \right)^\beta B_\nu (T_{\text{dust}}),\qquad(2)$$

where S_ν is the flux density, A the amplitude, ν the frequency, $\nu_0 = c/250\ \mu$m and B_ν is the Planck function. We fitted the model to the data using a χ^2 minimization routine, keeping β fixed at 1.5. The best-fit curve is shown in Fig. 5 together with the 95% confidence interval, and it corresponds to a dust temperature of $T_{\text{dust}} = 33 \pm 5$ K. Changing β between 1 and 2 results in changes in the derived dust temperature that are smaller than the 1σ confidence interval.

A more elaborate model must be used to fit the full SED, as the PACS data points fall outside the best-fit curve; however, our aim is not to accurately model the dust SED, but to derive a lower limit to the dust temperature. A second hotter dust component within the ISM of SMM J0658 could give rise to an excess power at wavelengths below 100 μm (the detection of hot molecular gas with $T \sim 375$ K (G10) indicates the possibility of a hot dust component in SMM J0658). Rex et al. (2010) used the LIRG templates of Rieke et al. (2009) to model the far-infrared/submm SED in SMM J0658. In Fig. 5 we show for reference the Rieke et al. template for a corresponding total far-infrared luminosity of $2 \times 10^{11}\ L_\odot$, magnified by a factor $\mu_{AB} = 100$, which fits the observed data better on the Wien side of the spectrum.

We can also use the Rieke et al. template to calculate the estimated continuum flux density for SMM J0658 in the two ATCA bands. The expected flux densities are <1 mJy in the 3 mm band and <50 μJy in the 7 mm band. This is below our detection limits and is consistent with our non-detection.

From the SED we also estimate the total mass of cold dust in SMM J0658. Following Papadopoulos et al. (2000), we calculate the dust mass from

$$M_{\text{dust}} = \frac{D_L^2\ (S_{870}/\mu_{AB})}{(1+z)\ k_d(\nu)} \left[B(\nu, T_{\text{dust}}) - B(\nu, T_{\text{CMB}}(z)) \right]^{-1}\qquad(3)$$

where ν is the rest frequency of the observed 870 μm emission, S_{870} is the 870 μm flux density, and $k_d = 0.04\ (\nu/250\ \text{GHz})^\beta$ is the dust emissivity function. As in the SED fitting, we used $\beta = 1.5$. Together with the dust temperature T_{dust} derived above and $T_{\text{CMB}}(z = 2.8) = 10.3$ K the dust mass is $M_{\text{dust}} = 1.1^{+0.8}_{-0.3} \times 10^7\ (\mu_{AB}/100)^{-1}\ M_\odot$, where the uncertainties are due to the uncertainty in the dust temperature. The systematic uncertainty in the normalization and shape of the dust emissivity function is not included. However, it is considerable and likely overshadows the uncertainties in the dust temperature.

4.2. Molecular and dynamical mass

In this section we estimate the molecular gas mass and the dynamical mass using the luminosity of the CO lines and their linewidth.

Using CO as a tracer of the more abundant H₂ molecule is the main method to infer the total molecular mass in a molecular cloud or an entire galaxy (e.g. Dickman et al. 1986). The relation between CO luminosity and molecular mass is then $M_{\text{gas}} = \alpha L_{\text{CO}}$, where the constant of proportionality, α, is ~4.6 $M_\odot$ (K km s^{-1} pc^2)$^{-1}$ for the $J = 1$–0 line in Galactic giant molecular clouds or nearby disk galaxies. For starburst galaxies (LIRGs and ULIRGs) α is considerably lower ($\alpha \sim 0.8\ M_\odot$ (K km s^{-1} pc^2)$^{-1}$, Solomon et al. 1997). The main reason for the difference is that in disk galaxies the molecular gas is distributed in individual virialized molecular clouds, whereas in the centers of starburst galaxies the CO emission originates from an extended medium and the CO linewidths are determined by the total dynamical mass in the region (Maloney & Black 1988; Solomon & Vanden Bout 2005). For a recent discussion of the influence of the physical conditions of the interstellar medium on the CO-to-H₂ conversion factor in luminous IR galaxies see, for instance, Papadopoulos et al. (2012a, 2012b).

Adopting $\alpha = 0.8\ M_\odot$ (K km s^{-1} pc^2)$^{-1}$, and using the luminosity of the combined CO(1–0) line displayed in Table 2, we find a gas mas of $M_{\text{gas}} = (1.8 \pm 0.3) \times 10^9\ (\mu_{AB}/100)^{-1}\ M_\odot$, where the uncertainties are 1σ and represent only the statistical uncertainty in the CO luminosity, not the systematic uncertainty in the value of α, which most likely dominates. Using $\alpha = 3.6 \pm 0.8\ M_\odot$ (K km s^{-1} pc^2)$^{-1}$ instead, as is appropriate for the Milky Way (e.g. Strong et al. 1988), nearby spiral galaxies (e.g. Maloney & Black 1988), and which has also been found in $z = 1.5$ BzK-galaxies (Daddi et al. 2010), for SMM J0658, the total gas mass is considerably larger, $M_{\text{gas}} = (8.1 \pm 1.3) \times 10^9\ (\mu_{AB}/100)^{-1}\ M_\odot$. Even with the latter value, SMM J0658 is a LIRG with low CO emission and a low gas mass, when compared to intrinsically brighter submm galaxies.

The dynamical mass can be estimated, assuming again that the CO line originates from an extended medium whose dynamics depend on the total enclosed mass, from

$$M_{\text{dyn}} = L\,\Delta V^2 / G,\qquad(4)$$

Table 3. Positions of counterparts of SMM J0658.

	$\Delta\alpha$ ($''$)	$\Delta\delta$ ($''$)	Reference
LABOCA (870 μm)	0.0	0.0	1
SABOCA (350 μm)[+]	$1.3 \pm 2.0 \pm 4.5$	$-0.7 \pm 2.0 \pm 4.5$	2
CO(1–0) (Image A)[*]	2.9 ± 0.4	4.0 ± 1.1	2
CO(1–0) (Image B)[*]	-3.9 ± 0.4	-6.0 ± 1.2	2
CO(3–2) (Image A)	2.9 ± 0.7	2.2 ± 0.5	2
CO(3–2) (Image B)	-2.4 ± 0.3	-0.9 ± 0.2	2
IRAC (Image A)[**]	3.2	2.8	3
IRAC (Image B)[**]	-4.4	-1.2	3

Notes. All angular offsets are stated relative to the LABOCA centroid (RA 06:58:37.62; Dec -55:57:04.8). [+] The first uncertainties come from the Gaussian fit and the second uncertainties are the pointing uncertainties. [*] We compared the astrometry of the CO(1–0) map to that of the HST image by measuring the position of the elliptical galaxy located 21$''$ south of SMM J0658. They agree within 1$''$. [**] The positions were taken from Gonzalez et al. (2009) who don't quote any uncertainties.

References. 1 – Johansson et al. (2010); 2 – This work; 3 – Gonzalez et al. (2009).

(e.g. Solomon & Vanden Bout 2005), where L is the size of the region where the CO emission originates from, ΔV is the full width at half maximum of the CO line, and G is Newton's constant.

Due to the moderate signal-to-noise ratio in our data, we refrain from estimating the size of the CO emitting region. However common values adopted for SMGs in the literature are $L \sim 1$–2 kpc (e.g. Kneib et al. 2005; Danielson et al. 2010). Using the linewidth of the CO(3–2) line, the dynamical mass is then $(1.3 \pm 0.4) \times 10^{10}$ $(L/1\,\text{kpc})$ $M_\odot$. Uncertainties are due to the uncertainty in the linewidth and do not include systematic uncertainties, which most likely dominate. Note that the dynamical mass is to first order independent of the gravitational magnification.

The properties of SMM J0658 are compared with those of other star-forming galaxies in Sect. 4.4.

4.3. Positional offsets

Offsets of a few arcseconds are seen between the positions of the CO detections and those of the two *Spitzer* images of SMM J0658, image A and image B. Those offsets are listed in Table 3, and are best seen in Fig. 6, which shows the HST WFC3 map of SMM J0658 in grey-scale[5]. To reveal the faint arc between the two *Spitzer* images, we subtracted a model of the foreground elliptical galaxy using the Galfit code (Peng et al. 2010). We masked out other bright objects near SMM J0658. The positions of the centroids of the SABOCA and LABOCA detections are shown. Their offset is within the uncertainties of the observations[6].

Contours of the integrated intensity images of CO(3–2) and CO(1–0) are also overlaid. No contour for the CO(3–2) signal close to image A is drawn because of the low significance of the detection. The CO(3–2) detection appears about 2$''$ to the east of the *Spitzer* western image (image B). The CO(1–0) detection, on the other hand, peaks about 5$''$ to the south of image B. The CO(1–0) is therefore shifted relative to the CO(3–2) by about 1.5$''$ in RA and 5$''$ in declination. Concerning image A,
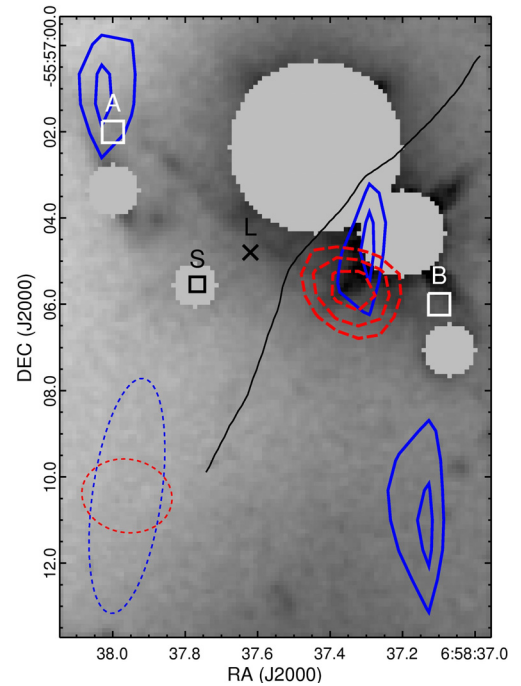

Fig. 6. HST image (G10) of SMM J0658 overlaid with the two *Spitzer* image positions A and B (white squares). The red and blue contours are the same as in Fig. 3, and show the CO(3–2) and CO(1–0) emission. We used GALFIT to subtract a model of the elliptical galaxy at $(\alpha_{2000}, \delta_{2000}) = (06$:58:37.44, -55:57:2.4) and masked the region of that galaxy, a nearby star and three other objects (gray disks). The faint arc between images A and B is visible, roughly orthogonal to the critical line shown in black (see Fig. 3 in G10 for a color image). The cross and box markers show the centroid of the LABOCA and SABOCA detections. The synthesized beams at 3 mm and 7 mm are shown in the bottom left corner as red and blue ellipses.

[5] Proposal identifier 11099, principal investigator M. Bradač; (G10).

[6] The positional accuracy when fitting two-dimensional Gaussians to sources superimposed on uncorrelated Gaussian noise can be written $\Delta x \simeq 0.6\,(\text{S/N})^{-1}$ FWHM (Condon 1997; Ivison et al. 2007). The accuracy in the fit for the SABOCA and LABOCA detections is thus 2$''$ and <1$''$ respectively. The pointing accuracy of both instruments is 2$''$ in azimuth and 4$''$ in elevation (Siringo et al. 2009, 2010).

a smaller offset of about 2$''$ is seen between the CO(1–0) and the faint CO(3–2) detections. There, the CO(1–0) seems to be shifted to the north of image A.

The positional accuracy of our CO(1–0) map has been checked using the position of the bright radio source 21$''$ south of SMM J0658, as described in Sect. 3.2.1; it agrees within one arcsecond with the position measured by Liang et al. (2000) in cm-wave ATCA observations and also with the *Spitzer* and HST positions.

Table 4. Summary and comparison of physical properties of SMM J0658 and other highly magnified SMGs.

Source	SMM J0658 (1)	SMM J16359+6612 (2)	SMM J2135−0102 (3)
Redshift	2.7793	2.5174	2.3259
Magnification	80–115	45 ± 3.5	32.5 ± 4.5
Submm flux density (mJy)	~0.5	~0.8^a	~3
$L_{CO(1-0)}$ (10^8 K km s^{-1} pc^2)	22.6 ± 3.6	–	173 ± 9
$L_{CO(3-2)}$ (10^8 K km s^{-1} pc^2)	12.7 ± 2.0	37 ± 2	117.6 ± 0.9
M_{gas} ($10^9\,M_\odot$)	1.8 ± 0.3	4.5 ± 1.0	14 ± 1
M_{dyn} ($10^9\,M_\odot$)	$(13 \pm 4)(L/1\mathrm{kpc})^b$	15 ± 3	$40 - 80$
L_{FIR} ($10^{12}L_\odot$)^c	0.3 ± 0.03	1.6 ± 0.4	2.3 ± 0.1
SFR ($M_\odot$ yr^{-1})	100–150	~500	400 ± 20
SFE ($L_\odot\,M_\odot^{-1}$)^d	170	~320	165 ± 7
M_{dust} ($10^7\,M_\odot$)	$1.1^{+0.8}_{-0.3}$	1.9 ± 0.3	~15
T_{dust} (K)	33 ± 5	51 ± 3	$(30; 57 \pm 3)^e$

Notes. All values have been corrected for the individual gravitational magnification factors. $^{(a)}$ Flux density measured at 850 μm; the other two flux densities were measured at 870 μm. For a submm spectral index of ~3 the flux difference between the two wavelengths is less than 3%. $^{(b)}$ L is the size of the CO-emitting region. $^{(c)}$ Rest-frame infrared luminosity between wavelengths $\lambda = 8$–1000 μm. $^{(d)}$ Star formation efficiency, defined as L_{FIR}/M_{gas}. $^{(e)}$ Dust temperatures for the extended and clumpy dust component reported by Danielson et al. (2010) for a two-phase model. (1) This work; (2) Kneib et al. (2004, 2005); (3) Danielson et al. (2010).

Clearly, deeper maps are needed to determine whether the observed offsets in SMM J0658 are real or due to a combination of pointing uncertainties, low signal-to-noise ratio, and the elongated CO(1–0) beam.

4.4. Physical parameters and comparison with other galaxies

Let us compare the properties of SMM J0658 with those of other galaxies, in particular the sub-mJy galaxy at $z \sim 2.5$ (SMM J16359+6612) studied by Kneib et al. (2005) and the brighter lensed galaxy at $z \sim 2.3$ (SMM J2135-0102) studied by Swinbank et al. (2010) and Danielson et al. (2010). Those are highly magnified galaxies with several similarities with SMM J0658.

Derived parameters for SMM J0658 and the two other galaxies are listed in Table 4. The intrinsic submm flux density of SMM J0658 is about 60% that of the $z \sim 2.5$ galaxy and ~6 times lower than that of the $z \sim 2.3$ galaxy. The ratios of the far-infrared luminosities are slightly different: the $z \sim 2.5$ galaxy is ~5 times more luminous, and the $z \sim 2.3$ galaxy is ~8 times more luminous. As expected, the amount of molecular gas in SMM J0658 is lower than in the two other galaxies. Interestingly, the star formation efficiency is comparable to that in the ULIRG at $z \sim 2.3$. The dust mass in SMM J2135-0102 is an order of magnitude larger than that in the two other galaxies. However, the gas to dust mass ratio, M_{gas}/M_{dust} is ~160 for SMM J0658, ~240 for SMM J16359+6612 and ~90 for SMM J2135-0102. Given the large systematic uncertainties in determination of the gas and dust mass, no trends can be identified from the gas to dust ratios.

How does SMM J0658 compare with larger samples of local and high-redshift LIRGs and ULIRGs? In Fig. 7 we show the CO-line luminosity versus the far-infrared luminosity for the three galaxies discussed above, and for the nearby luminous infrared galaxies of Yao et al. (2003) and Solomon et al. (1997) and the bright high-redshift submm galaxies of Ivison et al. (2011) and Harris et al. (2010) SMM J0658 falls on the general correlation and is the least FIR-luminous high-redshift galaxy in the diagram.

What is the possible duration of its starburst phase in SMM J0658? The star formation rate derived from the far-infrared SED is $100-150\,M_\odot$ yr^{-1} $[\mu_{AB}/100]^{-1}$ (G10). The
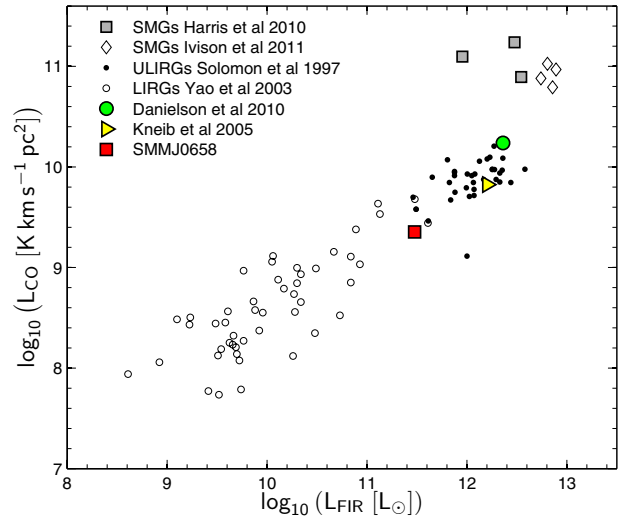

Fig. 7. Far-infrared luminosity versus CO(1–0) luminosity for the three galaxies summarized in Table 4: SMM J0658 (this study), SMM J16359+6612 (Kneib et al. 2005) and SMM J2135−0102 (Danielson et al. 2010). Local LIRGs and ULIRGs (Yao et al. 2003; Solomon et al. 1997) and high-redshift submm galaxies (Harris et al. 2010; Ivison et al. 2011) are also shown. Because SMM J16359+6612 has not been detected in CO(1–0), the CO(3–2) line luminosity was converted using $r_{31} = 0.6$ (which appears appropriate for SMGs, see Sect. 3.2.3). SMM J0658 is the least FIR-luminous high-redshift galaxy.

molecular gas mass divided by the star formation rate (M_{gas}/SFR) provides a measure of the possible duration of the starburst phase, or at least for how long the starburst phase can last at the current star formation rate and the current reservoir of molecular gas to form stars from. For SMM J0658 this ratio is 15 to 20 Myr. Note that the starburst duration is independent of the magnification factor. G10 fitted stellar population models to the near-infrared SED of SMM J0658 and found that models with a stellar population age <90 Myr or between 1.4 Gyr and 2.6 Gyr give the best fit to the data. They noted however that the large submm flux density is a strong argument for the lower age, an argument which is strengthened by the starburst duration calculated here.

One can estimate the gas mass fraction, $f_{gas} = M_{gas}/(M_{gas} + M_\star)$, from the gas mass derived from the CO lines and the stellar mass derived from near-infrared measurements. G10 gave $M_\star = 4 \times 10^9 (\mu_{AB}/100)^{-1} M_\odot$ and noted that systematic uncertainties can be a factor of 2 or larger, which makes them the largest source of uncertainty on the stellar mass. The influence of systematic uncertainties on derived stellar masses for near-infrared SEDs is discussed by Conroy et al. (2009). M_{gas} depends of course on the adopted value of the CO-to-H$_2$ conversion factor, α. For $\alpha \simeq 0.8\, M_\odot\,(\mathrm{K\,km\,s^{-1}\,pc^2})^{-1}$ (as in local ULIRGs), f_{gas} in SMM J0658 would be $31 \pm 12\%$. For $\alpha \simeq 3.6\, M_\odot\,(\mathrm{K\,km\,s^{-1}\,pc^2})^{-1}$ (as in the Milky Way or in nearby spirals, see Sect. 4.2), $f_{gas} \simeq 67 \pm 17\%$. Note that the uncertainties on the gas mass fractions derived here do not include the systematic uncertainty in the stellar mass determination. The fact that such a large fraction of the molecular gas has not yet been converted into stars is another argument in favor of a young system. Such high gas mass fractions are typical for high-redshift systems: Tacconi et al. (2010) found $f_{gas} \simeq 44\%$ in a sample of galaxies around $z \sim 2.3$. Despite the uncertainty in the adopted value of α, the gas mass fraction in SMM J0658 is large compared with local galaxies: for comparison, the gas fraction in a sample of local spiral galaxies is ~7% (Leroy et al. 2005).

5. Conclusions

This paper presents a study of the molecular gas and dust in one of the least massive high-redshift galaxies observed so far, the $z = 2.8$ submm galaxy SMM J0658 lensed by the Bullet Cluster.

– We detected for the first time rotational transitions of CO from SMM J0658. The CO(1–0) to CO(3–2) brightness temperature ratio is comparable to that observed in other high-redshift star-forming galaxies.
– We revise the redshift estimated by Gonzalez et al. (2010) from $z = 2.791 \pm 0.007$ to $z = 2.7793 \pm 0.0003$.
– The mass of cold molecular gas is estimated to be between 1/3 and 2/3 of the total baryonic mass.
– From the linewidths of the CO(3–2) transition we derive a dynamical mass of $(1.3 \pm 0.4) \times 10^{10}\, M_\odot$, for a CO-emitting disk with a physical size of 1 kpc.
– The derived molecular and dynamical masses are consistent with a galaxy less massive than the Milky Way. SMM J0658 is also less massive than most star-forming galaxies observed at high redshift so far (e.g. Tacconi et al. 2010; Greve et al. 2005; Swinbank et al. 2010).
– Using ground-based 350 μm imaging we detected continuum radiation from SMM J0658. The signal-to-noise ratio is only 3.6, but the detection makes it possible to confirm that the emission previously seen in the larger beams of BLAST and Herschel (Rex et al. 2009; Rex et al. 2010) comes from SMM J0658. The value of the flux density measured by SABOCA is consistent with the Herschel and BLAST values.
– Owing to the extremely high magnification, this galaxy is a target of choice for further studies of the properties of intrinsically faint high-redshift galaxies, for example with ALMA.

References

Alloin, D., Kneib, J., Guilloteau, S., & Bremer, M. 2007, A&A, 470, 53
Blain, A. W., Smail, I., Ivison, R. J., Kneib, J.-P., & Frayer, D. T. 2002, Phys. Rep., 369, 111
Bradač, M., Clowe, D., Gonzalez, A. H., et al. 2006, ApJ, 652, 937
Brown, R. L., & Vanden Bout, P. A. 1991, AJ, 102, 1956
Chapman, S. C., Richards, E. A., Lewis, G. F., Wilson, G., & Barger, A. J. 2001, ApJ, 548, L147
Chapman, S. C., Smail, I., Ivison, R. J., & Blain, A. W. 2002, MNRAS, 335, L17
Chapman, S. C., Neri, R., Bertoldi, F., et al. 2008, ApJ, 689, 889
Condon, J. J. 1997, PASP, 109, 166
Conroy, C., Gunn, J. E., & White, M. 2009, ApJ, 699, 486
Coppin, K. E. K., Swinbank, A. M., Neri, R., et al. 2008, MNRAS, 389, 45
Cowie, L. L., Barger, A. J., & Kneib, J.-P. 2002, AJ, 123, 2197
Daddi, E., Dannerbauer, H., Stern, D., et al. 2009, ApJ, 694, 1517
Daddi, E., Bournaud, F., Walter, F., et al. 2010, ApJ, 713, 686
Danielson, A. L. R., Swinbank, A. M., Smail, I., et al. 2010, MNRAS, 1565
Dannerbauer, H., Daddi, E., Riechers, D. A., et al. 2009, ApJ, 698, L178
Dickman, R. L., Snell, R. L., & Schloerb, F. P. 1986, ApJ, 309, 326
Egami, E., Rex, M., Rawle, T. D., et al. 2010, A&A, 518, L12
Gonzalez, A. H., Clowe, D., Bradač, M., et al. 2009, ApJ, 691, 525
Gonzalez, A. H., Papovich, C., Bradač, M., & Jones, C. 2010, ApJ, 720, 245
Greve, T. R., Bertoldi, F., Smail, I., et al. 2005, MNRAS, 359, 1165
Griffin, M. J., Abergel, A., Abreu, A., et al. 2010, A&A, 518, L3
Güsten, R., Nyman, L. Å., Schilke, P., et al. 2006, A&A, 454, L13
Harris, A. I., Baker, A. J., Zonak, S. G., et al. 2010, ApJ, 723, 1139
Hughes, D. H., Serjeant, S., Dunlop, J., et al. 1998, Nature, 394, 241
Ivison, R. J., Greve, T. R., Dunlop, J. S., et al. 2007, MNRAS, 380, 199
Ivison, R. J., Papadopoulos, P. P., Smail, I., et al. 2011, MNRAS, 412, 1913
Johansson, D., Horellou, C., Sommer, M. W., et al. 2010, A&A, 514, A77
Johansson, D., Sigurdarson, H., & Horellou, C. 2011, A&A, 527, A117
Kneib, J.-P., van der Werf, P. P., Kraiberg Knudsen, K., et al. 2004, MNRAS, 349, 1211
Kneib, J.-P., Neri, R., Smail, I., et al. 2005, A&A, 434, 819
Knudsen, K. K., van der Werf, P., Franx, M., et al. 2005, ApJ, 632, L9
Knudsen, K. K., Barnard, V. E., van der Werf, P. P., et al. 2006, MNRAS, 368, 487
Knudsen, K. K., van der Werf, P. P., & Kneib, J.-P. 2008, MNRAS, 384, 1611
Kovács, A. 2008, in SPIE Conf. Ser., 7020, 45
Leech, J., Isaak, K. G., Papadopoulos, P. P., Gao, Y., & Davis, G. R. 2010, MNRAS, 406, 1364
Leroy, A., Bolatto, A. D., Simon, J. D., & Blitz, L. 2005, ApJ, 625, 763
Liang, H., Hunstead, R. W., Birkinshaw, M., & Andreani, P. 2000, ApJ, 544, 686
Maloney, P., & Black, J. H. 1988, ApJ, 325, 389
Papadopoulos, P. P., Röttgering, H. J. A., van der Werf, P. P., et al. 2000, ApJ, 528, 626
Papadopoulos, P. P., van der Werf, P., Xilouris, E., Isaak, K. G., & Gao, Y. 2012a, ApJ, 751, 10
Papadopoulos, P. P., van der Werf, P., Xilouris, E. M., et al. 2012b, MNRAS, accepted [arXiv:1109.4176]
Peng, C. Y., Ho, L. C., Impey, C. D., & Rix, H. 2010, AJ, 139, 2097
Pérez-González, P. G., Egami, E., Rex, M., et al. 2010, A&A, 518, L15
Rex, M., Ade, P. A. R., Aretxaga, I., et al. 2009, ApJ, 703, 348
Rex, M., Rawle, T. D., Egami, E., et al. 2010, A&A, 518, L13
Riechers, D. A., Carilli, C. L., Walter, F., & Momjian, E. 2010, ApJ, 724, L153
Riechers, D. A., Walter, F., Carilli, C. L., et al. 2011, ApJ, 726, 50
Rieke, G. H., Alonso-Herrero, A., Weiner, B. J., et al. 2009, ApJ, 692, 556
Siringo, G., Kreysa, E., Kovács, A., et al. 2009, A&A, 497, 945
Siringo, G., Kreysa, E., De Breuck, C., et al. 2010, The Messenger, 139, 20
Smail, I., Ivison, R. J., & Blain, A. W. 1997, ApJ, 490, L5
Smail, I., Ivison, R. J., Blain, A. W., & Kneib, J.-P. 2002, MNRAS, 331, 495
Solomon, P. M., Radford, S. J. E., & Downes, D. 1992, Nature, 356, 318
Solomon, P. M., Downes, D., Radford, S. J. E., & Barrett, J. W. 1997, ApJ, 478, 144
Solomon, P. M., & Vanden Bout, P. A. 2005, ARA&A, 43, 677
Stanway, E. R., Bremer, M. N., Davies, L. J. M., et al. 2008, ApJ, 687, L1
Strong, A. W., Bloemen, J. B. G. M., Dame, T. M., et al. 1988, A&A, 207, 1
Swinbank, A. M., Smail, I., Longmore, S., et al. 2010, Nature, 464, 733
Tacconi, L. J., Genzel, R., Neri, R., et al. 2010, Nature, 463, 781
Walter, F., Carilli, C., & Daddi, E. 2010, Molecular Gas at High Redshift (Wiley-VCH Verlag GmbH & Co. KGaA), 167
Wardlow, J. L., Smail, I., Wilson, G. W., et al. 2010, MNRAS, 401, 2299
Weiß, A., Henkel, C., Downes, D., & Walter, F. 2003, A&A, 409, L41
Wilson, G. W., Hughes, D. H., Aretxaga, I., et al. 2008, MNRAS, 390, 1061
Wright, E. L. 2006, PASP, 118, 1711
Yao, L., Seaquist, E. R., Kuno, N., & Dunne, L. 2003, ApJ, 588, 771